ACS Catalysis

pubs.acs.org/acscatalysis Research Article

Boosting Singlet Oxygen Oxidation of Micropollutants at an Enzyme-like Bifunctional Single-Atom Catalyst Interface

Dezhi Kong, Yafei Fan, Feifei Wang, Fangyu Zhang, Qi Zhao, Zhaoli Sun, Jianfei Yao, Menghui Chu, Guo Wang, Guanyun Zhang,* Zhaoyong Guan,* Hua Sheng, and Yifeng Wang*

Cite This: ACS Catal. 2025, 15, 8174–8184 Read Online

ACCESS | Metrics & More | Article Recommendations | Supporting Information

ABSTRACT: Singlet oxygen ($^1O_2$) plays a critical role in oxidation reactions, yet improving its reactivity with substrates remains a significant challenge. This study reports an enzyme-like bifunctional catalyst, Co−N_2O_2/NC, which can efficiently activate peroxymonosulfate (PMS) with high selectivity and nearly quantitatively generates $^1O_2$ without producing other reactive oxygen species to achieve high reactivity. Notably, it significantly increases the bimolecular reaction rate constant between $^1O_2$ and waterborne micropollutants, as demonstrated by the over 1400-fold enhancement in 4-chlorophenol (4-CP) oxidation compared to that in the bulk solution. Enzyme-like catalytic kinetics were observed, with N-sites of the N-doped carbon support serving for activating 4-CP via interfacial electronic interactions, while Co activates PMS to generate $^1O_2$. The interfacial charge transfer lowers the energy barrier for $^1O_2$ to approach the aromatic ring of 4-CP, which is the rate-limiting step in the oxygenation reaction. Our findings lay the foundation and offer guidance for designing catalysts that facilitate the efficient generation and use of $^1O_2$, expanding its application to a broader range of oxidation processes.

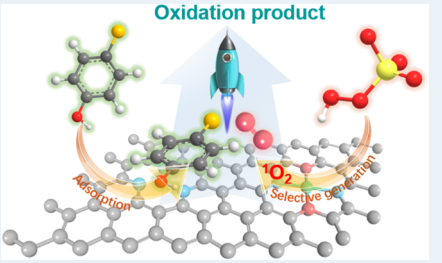

KEYWORDS: *single-atom catalyst, singlet oxygen, advanced oxidation technology, interfacial interaction, micropollutants*

1. INTRODUCTION

Singlet oxygen ($^1O_2$), the most important excited state of molecular oxygen, is a widely recognized oxidant of long-standing interest. It plays an important role in biological[1,2] and environmental processes[3−5] and has been extensively explored for antimicrobial applications,[6] as well as the selective oxygenation of alkenes, sulfides, and phosphines.[7−9] Moreover, due to its relatively longer lifetime and higher tolerance to environmental disturbance compared to free-radical reactive oxygen species (ROS, such as $^{\bullet}OH$, $SO_4^{\bullet-}$, and $O_2^{\bullet-}$), $^1O_2$ has also been considered to hold significant promise for the removal of low-concentration micropollutants in wastewater.[10−14] $^1O_2$ can be generated through various natural routes; for example, humic acid efficiently photosensitizes O_2 into $^1O_2$ under sunlight.[15] However, in chemical transformations, efficient strategies for $^1O_2$ formation are still lacking, with only a few methods available. Compared to traditional approaches like the photosensitization[16] of O_2 and the HOCl oxidation of H_2O_2,[17] recent advancements in Fenton-like catalysis using recyclable heterogeneous catalysts, particularly single-atom catalysts (SACs), to activate low-cost oxidants offer a promising route for the highly selective generation of $^1O_2$.[18−20] This emerging strategy has proven effective in removing waterborne pollutants for wastewater remediation and shows potential for selective oxidation in the synthesis of value-added fine chemicals recently.[21,22] Nonetheless, although a few systems can generate $^1O_2$ with nearly 100% selectivity, the activity of the catalysts remains unsatisfying.[23] Moreover, a critical yet often overlooked constraint of $^1O_2$ lies in its inherently modest oxidation potential (E = 0.34 V for $^1O_2/O_2^{\bullet-}$ in water),[24] short lifetime (microseconds in water),[25] low yield (sub-nM concentrations),[26] and limited diffusion distance.[27] Consequently, its reactivity in bimolecular reactions with target substrates in a bulk solution is generally low. For instance, in the Rose Bengal (RB, sodium salt) photosensitization system, the second-order rate constant between $^1O_2$ and 4-chlorophenol (4-CP) is merely ca. 10^6 M^{-1} s^{-1},[28] which is significantly lower than that of a diffusion-controlled bimolecular reaction.[29] While pollutant degradation in heterogeneously catalyzed peroxymonosulfate (PMS)-based systems is often rapid (typically within 30 min), the suspected sluggish reactivity of $^1O_2$ has sparked debate about its actual role in these systems. In this context, to strengthen the roles of $^1O_2$ in oxidative processes, it is crucial not only to enhance its production but also to improve its reactivity with target molecules.

With the above analyses in mind, in this study, we explore a Co−N_2O_2/NC single-atom catalyst for activating PMS to generate $^1O_2$ and enhancing the bimolecular reaction between

Received: February 24, 2025
Revised: April 23, 2025
Accepted: April 24, 2025

https://doi.org/10.1021/acscatal.5c01429
ACS Catal. 2025, 15, 8174−8184

$^1O_2$ and micropollutants. Nitrogen-doped carbon (NC) is a widely studied catalytic support material due to its abundance, high stability, and environmental compatibility.[30,31] The incorporation of N-dopants generates coordination sites that can anchor various metal ions within the two-dimensional (2D) layered C-based matrix, rendering it an ideal support for metal SACs.[32] Furthermore, by controlling the number of coordinating N atoms at the metal centers, the catalytic activity of SACs can be readily optimized.[33,34] While substantial progress has been made in developing NC-supported SACs with versatile metal coordination, the role of the NC support in catalysis has received comparatively less attention. Also, an SAC with Co−N_2O_2 coordination has yet to be explored for activating PMS to generate $^1O_2$. Here, we reveal that Co−N_2O_2/NC functions as an enzyme-like bifunctional catalyst, where the Co sites effectively activate PMS to generate $^1O_2$, and the N-sites on the NC support activate 4-CP via strong electronic interactions, thus enhancing the reactivity of 4-CP toward $^1O_2$ attack. Remarkably, Co−N_2O_2/NC achieved a 1400-fold increase in the second-order rate constant for the oxygenation reaction of 4-CP by $^1O_2$, compared to that of the homogeneous reaction. Our findings may provide a foundation for strengthening the application of $^1O_2$ in a broader range of chemical transformations and offer insights for designing next-generation catalysts capable of efficiently and selectively producing $^1O_2$ through PMS or H_2O_2 activation.

2. MATERIALS AND METHODS

2.1. Chemicals and Materials. Amorphous fumed SiO_2 powder was purchased from Alfa Aesar. *O*-Phenylenediamine, *p*-benzoquinone (*p*-BQ), $Co(NO_3)_2{\cdot}6H_2O$, 4-CP, furfural (FFA), *tert*-superoxide dismutase, phenol, 1,4-dichlorophenol (DCP), acetaminophen (APAP), sulfamethoxazole (SMX), rhodamine B (RhB), methylene blue (MB), PMS ($KHSO_5{\cdot}0.5KHSO_4{\cdot}0.5K_2SO_4$), methyl phenyl sulfoxide (PMSO), methyl phenyl sulfone ($PMSO_2$), 1,3-diphenylisobenzofuran (DPBF), benzoic acid (BA), and p-hydroxybenzoic acid (p-HBA) were purchased from Macklin. Methanol, *tert*-butanol alcohol, isopropanol, KCl, $MgCl_2$, $NaHCO_3$, KH_2PO_4, $Ca(NO_3)_2{\cdot}4H_2O$, NaOH, and H_2SO_4 were purchased from Sinopharm Chemical Reagent Co. Dimethyl sulfoxide (DMSO), humic acid, RB, nitro-blue tetrazolium (NBT), 2,2,6,6-tetramethyl-4-piperidone (TEMP), and 5,5-dimethyl-1-pyrroline-1-oxide (DMPO) were purchased from Aladdin. Fluorescein sodium (FS) was purchased form Adamas. All chemicals were used without any further purification.

2.2. Preparation of Catalysts. Previously, amine quinone polymerization has been used for the synthesis of single-atom catalysts.[35,36] Herein, the synthesis of our Co−N_2O_2/NC material draws upon the methods outlined in these references. First, 1.0 g of *p*-BQ was dissolved in 50 mL of ethanol. To this solution were added 1.0 g of SiO_2 and 0.3 g of $Co(NO_3){\cdot}6H_2O$, and the mixture was stirred for 10 min. Next, 15 mL of *o*-phenylenediamine (0.33 g) was added dropwise. The polymerization reaction was carried out at room temperature for 24 h to form polyamine quinone. After filtration, the solid product was washed with water and ethanol and then dried. The obtained precursor material was heated to 800 °C at a rate of 5 °C min^{-1} and carbonized for 2 h under a N_2 atmosphere. The resulting products were then treated with 100 mL of 2.0 M NaOH and 2.0 M H_2SO_4 solutions for 12 h to remove the SiO_2 template and any residual nanoparticles, respectively. Finally, Co−N_2O_2/NC was obtained by washing the plate with water. The preparation methods for other samples, including Co−N_4/NC, Co metal nanoparticles/NC (Co-NPs/NC), and NC are provided in the Supporting Information.

2.3. Characterization. X-ray diffraction (XRD) patterns were recorded by using a D8 Advanced X-ray diffractometer using a Cu Kα radiation source (λ = 0.15418 nm). X-ray photoelectron spectroscopy (XPS, ThermoFisher, ESCALAB 250Xi) was conducted with Al Kα ray ($h\nu$ = 1486.6 eV) as the excitation source. Nitrogen adsorption−desorption isotherms were measured using a Micromeritics ASAP 2460 analyzer at 77 K, and the specific surface area and porosity were calculated via the Barrett−Emmett−Teller and Barrett−Joyner−Halenda methods. The metal content and ion leaching were analyzed by inductively coupled plasma-mass spectrometry (ICP-MS, NexION 350X). Transmission electron microscopy (TEM, FEI Talos F200S) was performed at 200 kV, and scanning electron microscopy (SEM, TESCAN MIRA LMS) was conducted at 3 kV. Aberration-corrected high-angle annular dark-field scanning transmission electron microscopy (AC-HAADF-STEM, Titan Cubed Themis G2300) and EDS mapping were performed at 300 kV. In situ Raman spectra were recorded using a HORIBA Scientific LabRAM HR Evolution Raman spectrometer with a 532 nm laser. Free radicals were detected by electron paramagnetic resonance (EPR, JES-X320) at room temperature. Total organic carbon (TOC, Shimadzu-TOC-L) was measured to assess the mineralization efficiency during degradation reactions. X-ray absorption fine structure analysis was carried out at the BL11B beamline of the Shanghai Synchrotron Radiation Facility (SSRF), utilizing Si(111) crystal monochromators. Spectral analysis was performed using Athena and Artemis software. The detailed procedures of the EPR tests, ROS quantitation, and theoretical calculations are provided in the Supporting Information.

2.4. Degradation Reaction Procedure. In the PMS system, all pollutant degradation experiments were conducted in magnetically stirred beakers placed in a water bath (25 ± 0.5 °C). Typically, 5 mg of catalyst was first ultrasonically dispersed in 30 mL of a solution containing 0.625 mM 4-CP. Then, 10 mg of PMS was added to initiate the reaction. The reaction pH was 6.8, without any further adjustment. At predetermined time intervals, 1 mL of the reaction solution was filtered through a 0.22 μm poly(ether sulfone) filter and analyzed by high-performance liquid chromatography (HPLC, Shimadzu) using a C18 reversed-phase column (250 mm × 4.2 mm, 5 μm). 4-CP concentrations were determined with a mobile phase of acetonitrile/water (50:50, v/v) at a total flow rate of 1 mL min^{-1} with detection at λ = 279 nm.

In a dye-visible-light system, the micropollutant degradation was performed in a 50 mL quartz beaker. Specifically, 0.05 mM dye (RB, MB, or FS) was added to 30 mL of a solution containing 0.625 mM 4-CP. After stirring for 30 min in the dark, the reaction was initiated by turning on a 400−800 nm lamp. At predetermined time intervals, 1 mL of the reaction solution was filtered through a 0.22 μm poly(ether sulfone) filter and analyzed by HPLC. The subsequent analytical procedures were consistent with those described above. Here, the container, volume of the reaction solution, initial reaction pH, and reaction temperature were identical to those in the previous PMS system, ensuring comparability of the experimental results.

To assess the environmental stability of the catalysts, various parameters, such as impurity inorganic ions, temperature, pH,

https://doi.org/10.1021/acscatal.5c01429
ACS Catal. 2025, 15, 8174−8184

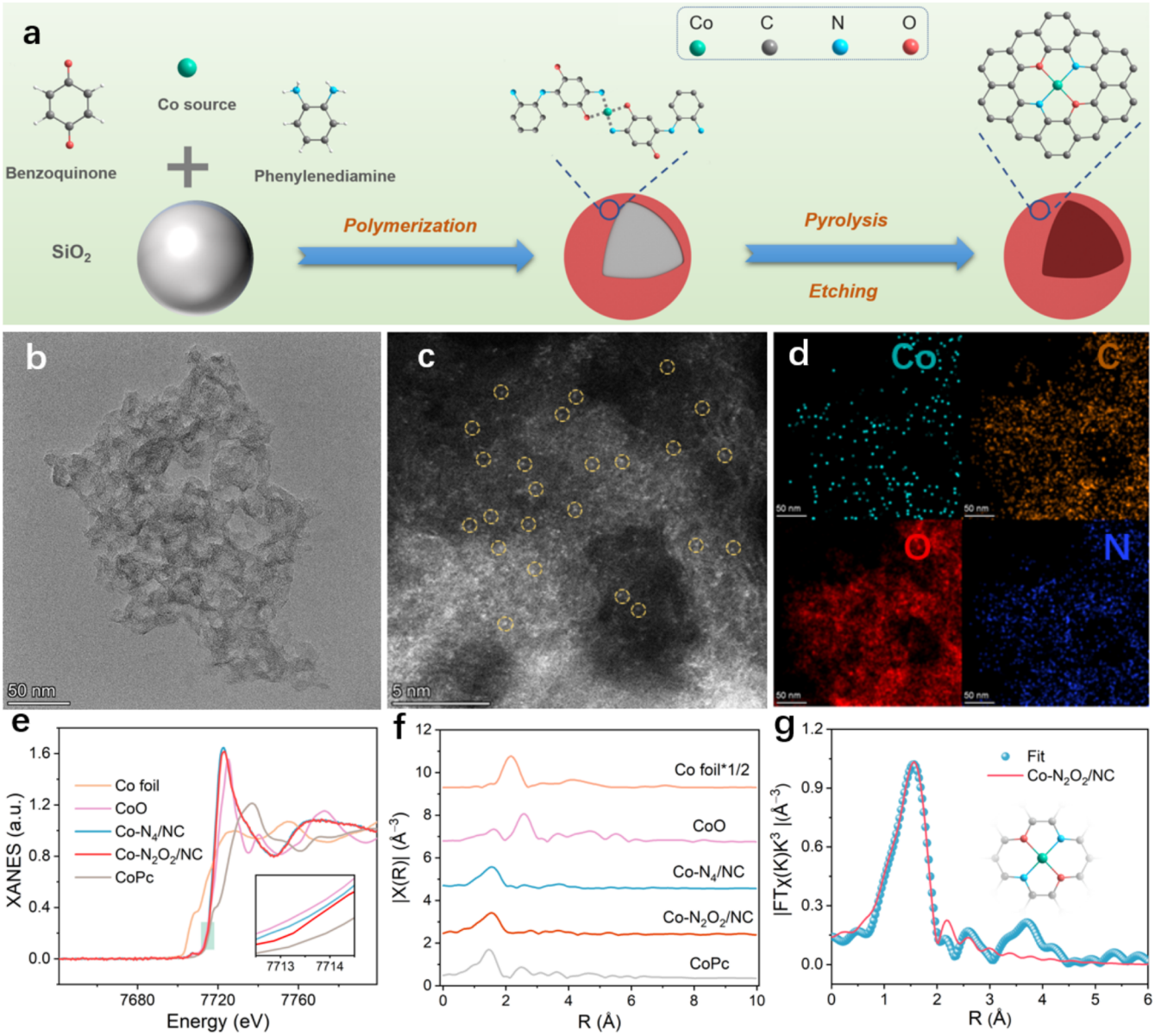

Figure 1. Synthesis, morphology, and coordination structure characterization. (a) Schematic diagram of the synthesis of Co−N_2O_2/NC. (b) TEM image, (c) AC-HAADF-STEM image, and (d) EDS mapping of Co−N_2O_2/NC. (e) XANES and (f) EXAFS spectra of the Co K-edge. (g) EXAFS fitting curves in the R-space of Co−N_2O_2/NC.

and water matrix, were controlled. The pH was adjusted using NaOH or H_2SO_4. Degradation reactions for different pollutants followed the same procedure as that for the 4-CP system. After each cycle, the recycled catalyst was washed, dried, and used in subsequent tests. All experiments were conducted in triplicate to ensure the reliability and reproducibility of the results.

3. RESULTS AND DISCUSSION

3.1. Preparation and Characterization of the Catalysts. Co−N_2O_2/NC comprises Co atoms dispersed on N-doped carbon, where Co is coordinated with two N atoms and two O atoms (Figure 1a). To synthesize it, o-phenylenediamine was added to a suspension of 1,2-quinone, $Co(NO_3)_2 \cdot 6H_2O$, and SiO_2. During the quinone-amine copolymerization on the SiO_2 template surface, Co^{2+} was captured in situ by the amino groups of the copolymer. The resulting preassembly was isolated via centrifugation, lyophilized, calcined at 800 °C under a N_2 atmosphere, and sequentially etched with NaOH to remove SiO_2 and H_2SO_4 to eliminate loosely bound Co species. The as-prepared sample was then thoroughly characterized with a variety of complementary techniques. ICP-MS and elemental analysis revealed the Co, C, and N contents in the sample to be 2.40, 79.9, and 11.0 wt %, respectively. The XRD pattern showed a broad peak around 23° (002 plane), characteristic of graphitic carbon, while Raman spectroscopy revealed D and G bands at approximately 1340 and 1580 cm^{-1} with an intensity ratio of 1:1, indicating a high degree of graphitization (Figure S1). XPS analysis identified three types of nitrogen species: graphitic-N, pyridinic N, and pyrrolic N (Figure S2). N_2 adsorption−desorption measurements indicated a high surface area of 595 $m^2\ g^{-1}$ (Figure S3 and Table S1). SEM and TEM images showed a porous, vesicle-like morphology without observable NPs or

https://doi.org/10.1021/acscatal.5c01429
ACS Catal. 2025, 15, 8174−8184

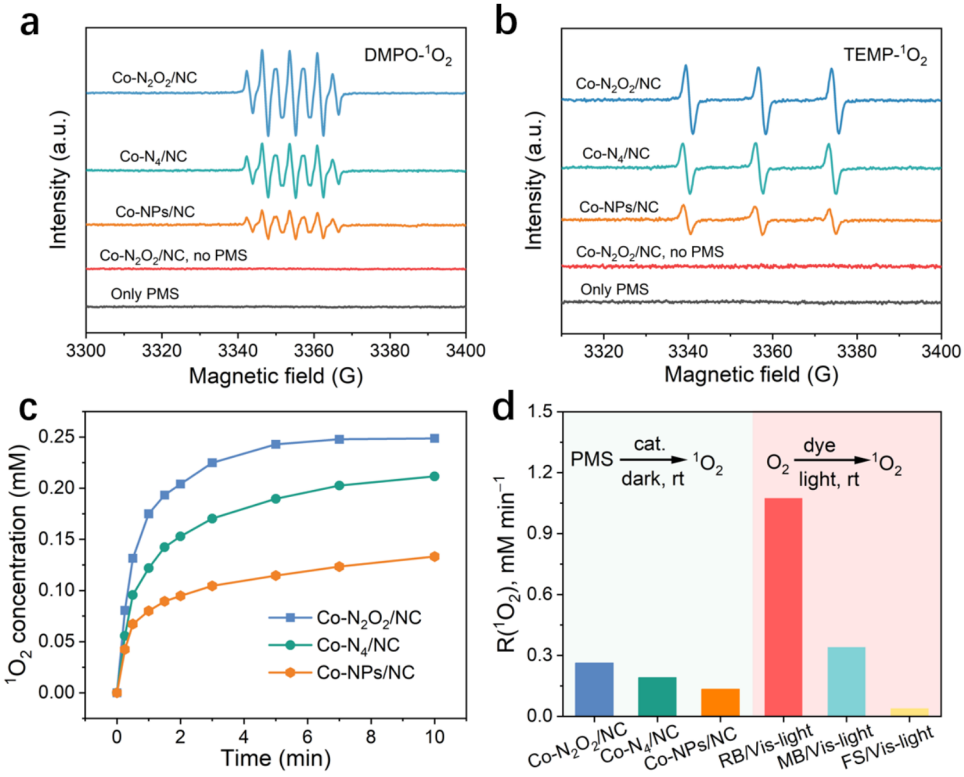

Figure 2. Detection and quantification of $^1O_2$. (a) DMPO spin-trapping EPR spectra for DMPO–$^1O_2$ in the Co–N_2O_2/NC/PMS system. (b) TEMP spin-trapping EPR spectra for TEMP–$^1O_2$ in the Co–N_2O_2/NC/PMS system. (c) Quantification of $^1O_2$ formation in the various systems using DPBF as the probe. (d) Comparison of $R(^1O_2)$ in the catalyst/PMS and dye/visible-light systems. The unspecified conditions were as follows: catalyst, 5 mg; PMS, 10 mg; DPBF, 0.25 mM; pH = 6.9; T = 298 K.

clusters (Figures 1b and S4). AC-HAADF-STEM and EDS elemental mapping images confirmed the uniform dispersion of Co as single atoms on the NC support (Figure 1c,d).

To access the structural and catalytic properties, three reference samples were prepared. Co–N_4/NC, with the classical Co–N_4 coordination environment of Co-based SACs, has previously been synthesized using other methods such as impregnation-calcination[37] or microwave heating.[38] Herein, it was synthesized using the preassembly calcination method analogous to that of Co–N_2O_2/NC but with 1,4-diaminobenzene as the precursor. This consistent synthesis approach ensured that Co–N_4/NC and Co–N_2O_2/NC had similar structural parameters, differing only in their Co coordination environment. A blank NC support was synthesized analogously but without added Co salts, while Co-NPs/NC was obtained by loading Co-NPs onto the as-prepared blank NC support (details in the Supporting Information). All three reference samples exhibited BET surface areas, crystallinity, graphitization degree, nitrogen species distribution, and support morphologies similar to those of Co–N_2O_2/NC (Figures S1–S6 and Tables S1 and S2). Electron microscopy confirmed atomically dispersed Co sites in Co–N_4/NC (Figure S7), whereas Co-NPs/NC contained abundant cobalt oxide NPs (Figure S6).

To elucidate the electronic state and coordination structure of Co single atoms, X-ray absorption near-edge structure (XANES) and extended X-ray absorption fine structure (EXAFS) were conducted on Co–N_2O_2/NC and Co–N_4/NC. The Co absorption edge position of Co–N_2O_2/NC is situated between CoO and cobalt(II) phthalocyanine (CoPc), indicating a Co valence state close to +2 (Figure 1e). However, the slightly lower edge position of Co–N_2O_2/NC compared to that of Co–N_4/NC is noted, implying a lower valence state of Co in the former. This finding is consistent with the XPS results (Figure S8), suggesting distinct coordination environments of Co in the two materials.[31] The EXAFS spectrum of Co–N_2O_2/NC displays a strong peak at 1.54 Å but no peaks characteristic of Co foil (2.16 Å) or CoO (2.58 Å), confirming that Co is atomically dispersed rather than NPs or clusters, consistent with the AC-HAADF-STEM image. The peak position, located between the reference values of Co–N and Co–O, suggests a mixed Co–N and Co–O coordination environment. In contrast, although Co–N_4/NC exhibits a similar peak at 1.54 Å, the EXAFS spectra of Co–N_4/NC and Co–N_2O_2/NC diverge significantly in the 2–8 Å range (Figure 1f). Additionally, the wavelet-transform spectrum of Co–N_2O_2/NC shows an absorption maximum at 3.95 Å, whereas Co–N_4/NC shows its peak at 3.84 Å (Figure S9), further confirming the differences in the Co coordination environments. The best fitting of the R-space spectrum indicates that nearly four atoms coordinate with the Co atoms in the first coordination shell for both Co–N_2O_2/NC and Co–N_4/NC. In conclusion, for Co–N_2O_2/NC, the polyamine quinone precursor induces dual Co coordination with N and O, with coordination numbers of 2.1 ± 0.1 for N and 2.0 ± 0.1 for O (Figure 1g). In contrast, Co–N_4/NC exhibits a purely Co–N coordination, with a coordination number of 4.3 ± 0.1 (Table S3).

3.2. Catalytic Formation of $^1O_2$. The catalytic performance of Co–N_2O_2/NC and the reference catalysts was evaluated in activating PMS for the oxidative degradation of 4-CP and other waterborne micropollutants. First, we assessed

https://doi.org/10.1021/acscatal.5c01429
ACS Catal. 2025, 15, 8174–8184

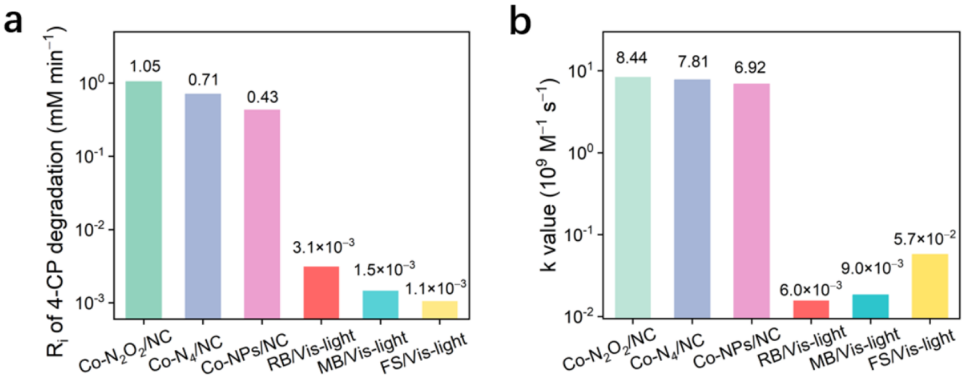

Figure 3. Comparison of the 4-CP degradation performance. Comparison of (a) R_i and (b) k values of 4-CP in the different systems.

their ability to activate PMS and generate $^1O_2$. Spin-trapping EPR spectroscopy was used to detect the ROSs by determining the characteristic signals of the spin adducts. As shown in Figure 2a, when DMPO was used as the spin trap, a very strong characteristic septet signal (assigned as DMPOX[33]) was observed in the Co−N_2O_2/NC system implying that DMPO may be oxidized by $^1O_2$.[30,39] Similarly, the TEMP−$^1O_2$ signal (Figure 2b), with a 1:1:1 intensity ratio, was also detected, further verifying the $^1O_2$ generation. $^1O_2$ generation was also observed in both the Co−N_4/NC and Co-NPs/NC systems, but the intensity of the signals was lower compared to that in the Co−N_2O_2/NC system, demonstrating that the activity of the catalysts in generating $^1O_2$ follows the order Co−N_2O_2/NC > Co−N_4/NC > Co-NPs/NC.

Subsequently, we employed a variety of chemical probes to quantify the production of $^1O_2$ and other ROS. It has been known that the selective oxidation of DPBF to 1,2-dibenzoylbenzene (DBB; Figure S10) by $^1O_2$ can be used to quantify $^1O_2$.[39] By this method, the initial rates of $^1O_2$ production (denoted as R($^1O_2$), the rate equation in the Supporting Information) in the Co−N_2O_2/NC, Co−N_4/NC, and Co-NPs/NC systems were measured to be 0.263, 0.191, and 0.134 mM min^{-1}, respectively (Figures 2c and S11). After complete PMS decomposition, the final $^1O_2$ yields were 0.248, 0.216, and 0.125 mM. In contrast, no characteristic products of $^{\bullet}$OH, $SO_4^{\bullet-}$, $O_2^{\bullet-}$, or Co^{IV}=O were detected for the three systems when using BA, p-HBA, NBT, or PMSO as probes, respectively (Figure S12),[40] suggesting either the absence of these ROSs or their concentrations being below the detection limits, consistent with the spin-trapping EPR results. Based on the above results, Co−N_2O_2/NC exhibits nearly 100% selectivity for $^1O_2$ generation during PMS activation, with significantly higher activity and selectivity than the reference catalysts Co−N_4/NC and Co-NPs/NC. To the best of our knowledge, Co−N_2O_2 is among the few catalysts capable of almost quantitatively converting PMS to $^1O_2$.[10,13,21,39] Since NC differs from Co−N_2O_2/NC only by the absence of Co single atoms, and the $^1O_2$ yield by NC is nearly zero, Co serves as the active site for $^1O_2$ generation. Moreover, the $^1O_2$ generation kinetics exhibit no distinguishable differences under O_2, N_2, or air atmospheres, indicating that $^1O_2$ originates from the decomposition of PMS, rather than from oxygen in the air (Figure S13).

To compare the $^1O_2$ generation activities, we selected three visible-light-responsive dyes commonly used for photosensitized $^1O_2$ production under homogeneous conditions: the cationic MB (chloride salt) and the anionic FS (sodium salt) and RB. Under visible-light irradiation, $^1O_2$ production by these dyes increased almost linearly over time (Figure S14). The initial $R(^1O_2)$ values are compared in Figure 2d. The values for MB and RB are 4.2 and 1.3 times higher, respectively, than that of the Co−N_2O_2/NC/PMS system, whereas FS exhibited a lower $R(^1O_2)$ than that of the Co−N_2O_2/NC/PMS system.

3.3. Reaction Rate of $^1O_2$ and 4-CP. To assess the reaction between $^1O_2$ and 4-CP, we utilized the above systems for $^1O_2$ generation and measured the reaction rate constants for $^1O_2$ and 4-CP (as well as other micropollutants) in each system. The degradation kinetics indicate that Co−N_2O_2/NC activated PMS to completely degrade 4-CP within 5 min (Figure S15). Figure 3a compares the initial degradation rates (R_i) of catalysts, revealing that Co−N_2O_2/NC exhibits faster degradation kinetics than Co−N_4/NC, Co-NPs/NC, and NC. Table S4 shows that compared to state-of-the-art catalysts, Co−N_2O_2/NC is among the most active Fenton-like catalysts currently available.

After 30 min of reaction, the Co−N_2O_2/NC system achieved a 74% removal of TOC and a 40% yield of Cl^- (Figure S16). HPLC and mass spectroscopy analysis revealed that the degradation products of 4-CP include *p*-BQ, 4-chlorocatechol, and several organic acids. The concentrations of these products initially increased, then decreased, and ultimately disappeared (Figures S17 and S18). Additionally, thermogravimetric analysis, Raman spectra, XRD, XPS, and electron microscopy characterization of the recovered Co−N_2O_2/NC after five cycles were comparable to that of the fresh sample (Figure S19). These results indicate that 4-CP undergoes degradation and partial mineralization, rather than polymerization and deposition on the catalyst surfaces.[32,41] Based on the successful degradation of 4-CP in the Co−N_2O_2/NC/PMS system, we assessed its practical application potential (Figure S20). First, the system completely removed several micropollutants, including MB, RhB, phenol, DCP, APAP, and SMX, within 10 min. Moreover, the system efficiently degraded 4-CP in the presence of common ions (Cl^-, NO_3^-, HCO_3^-, $H_2PO_4^-$, CO_3^{2-}, SO_4^{2-}), various water matrices (river water, lake water, spring water, seawater, and wastewater), and across a broad pH range (2−11) and temperature range (0−60 °C), demonstrating its robustness against common environmental challenges. The system also displayed excellent cycling stability (Figure S19). Finally, we fabricated a prototype membrane reactor by immobilizing Co−N_2O_2/NC on a porous poly(tetrafluoroethylene) membrane for continuous flow water treatment (Figure S21). To directly visualize the degradation

https://doi.org/10.1021/acscatal.5c01429
ACS Catal. 2025, 15, 8174−8184

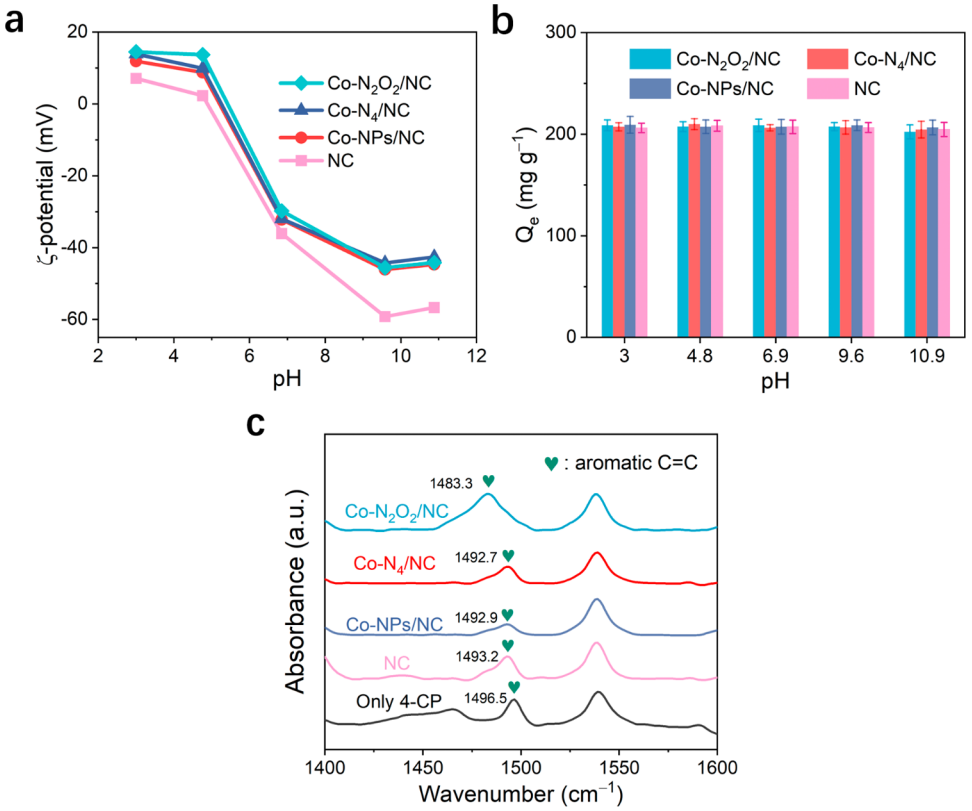

Figure 4. Adsorption behavior of 4-CP on different catalysts. (a) ζ-Potential and (b) Q_e of Co−N_2O_2/NC, Co−N_4/NC, Co-NPs/NC, and NC at different pH. (c) In situ FTIR spectra of 4-CP adsorbed on different catalysts. The peak at 1540 cm^{-1} is assigned to the instrument background signal.

efficiency, RhB was used as a model pollutant instead of 4-CP. To our delight, the effluent became completely colorless, indicating that the Co−N_2O_2/NC membrane effectively degraded RhB with minimal Co^{2+} leaching (<0.14%).

Our quenching experiments systematically excluded the involvement of other reactive ROS (including $SO_4^{\bullet-}$, $^{\bullet}OH$, $O_2^{\bullet-}$, and Co^{IV}=O), confirming that $^1O_2$ plays the dominant role in the degradation reaction of 4-CP in the Co−N_2O_2/NC/PMS system (Figure S22; see the discussion in the Supporting Information). Recent studies have also reported that PMS activation by certain catalysts selectively generates $^1O_2$ as the primary ROS for the oxidative degradation of 4-CP, resulting in high mineralization efficiency, a conclusion consistent with our findings.[10] In contrast, Yu et al.[32] reported that Co-SA supported on g-C_3N_4 activated PMS to degrade phenol, resulting in 100% polymerization, which subsequently deposited on the catalyst's surfaces. Similarly, Zhang et al.[34] employed MnN_5 to activate PMS for 4-CP degradation and found that oligomers of 4-CP formed. The fundamental difference in reaction pathways may arise from the distinct active ROS generated in each system, with their system producing high-valent metal-oxo species, while ours generated $^1O_2$.

We also employed the aforementioned three dyes to photosensitize the generation of $^1O_2$ under visible light for the degradation of 4-CP. Previous studies have shown that $^1O_2$ was the genuine oxidant in the aerobic dye-sensitized photooxygenation of phenols.[42−45] Here, the three dyes photosensitized the degradation of 4-CP, generating intermediates such as p-benzoquinone, similar to those observed in the Co−N_2O_2/NC/PMS system (Figure S23). Spin-trapping EPR and quenching experiments revealed that $^1O_2$ was also the dominant ROS in these homogeneous systems (Figures S24 and S25), consistent with the literature reports,[28,42,45] indicating the ability of $^1O_2$ to degrade phenolic pollutants. However, despite the significantly higher generation rates of $^1O_2$ in the dye/visible-light systems, the degradation of 4-CP was much lower than that in the heterogeneous Co−N_2O_2/NC/PMS system (Figure 3a). This implies that Co−N_2O_2/NC must enhance the bimolecular reaction between $^1O_2$ and 4-CP. To access this, the rate equation for the bimolecular reaction between $^1O_2$ and 4-CP is defined as follows[28]

$$R_i = -dC/dt = k \times C_e \times C(^1O_2) \quad (1)$$

where k is the second-order rate constant, C_e is the equilibrium concentration of 4-CP in the bulk solution, and $C(^1O_2)$ is the concentration of $^1O_2$. When comparing the kinetics of the dye/visible light and the Co−N_2O_2/NC/PMS systems, the following equation holds true

$$k(2) = \frac{R_i(2)/R(^1O_2, 2)}{R_i(1)/R(^1O_2, 1)} \times k(1) \quad (2)$$

where labels 1 and 2 are used to distinguish the parameters of the two systems. According to Tratnyek and Hoigne, when RB was used as a photosensitizer to generate $^1O_2$, the value of k is 6.0×10^6 M^{-1} s^{-1}.[28] This, in combination with the data reported in Figure 3a, the bimolecular rate constant between $^1O_2$ and 4-CP in the Co−N_2O_2/NC/PMS system can be calculated, as illustrated in Figure 3b.

Among the three heterogeneous systems, Co−N_2O_2/NC exhibits the highest k value, indicating its superior catalytic

https://doi.org/10.1021/acscatal.5c01429
ACS Catal. 2025, 15, 8174−8184

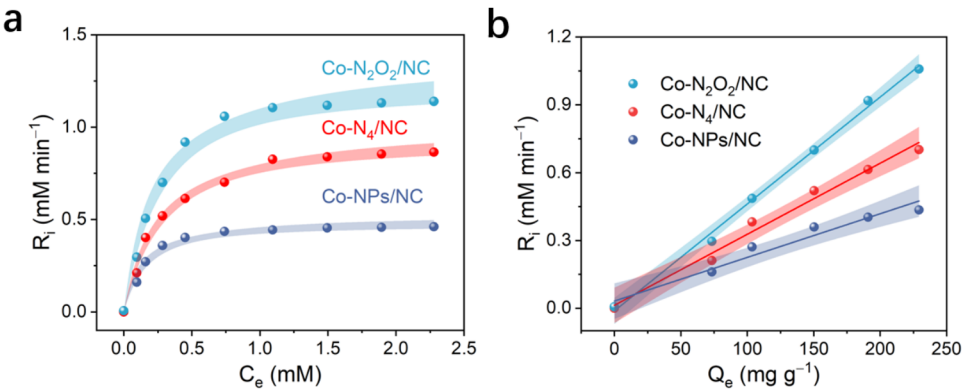

Figure 5. Enzymatic reactions involved in the degradation of micropollutants at the catalysts' interface. (a) Relationship between R_i and C_e of 4-CP. (b) Relationship between R_i and Q_e of 4-CP. The confidence bands are shown as shaded areas.

activity in promoting the reaction between $^1O_2$ and 4-CP. This further indicates that Co−N_2O_2/NC not only generates $^1O_2$ at the highest rate but also accelerates the reaction between $^1O_2$ and 4-CP more effectively. Additionally, when comparing the Co−N_2O_2/NC/PMS system with the three dye/visible-light systems, although the former has a much lower $R(^1O_2)$ than the RB/vis-light and MB/vis-light systems, its initial degradation rate (R_i) is significantly higher (Figure 3a). The k value of the Co−N_2O_2/NC/PMS system is 1407, 938, and 148 times higher than that of the FS/vis-light, RB/vis-light, and MB/vis-light systems, respectively (Figure 3b). Hence, the presence of the reaction interface in the heterogeneous system significantly enhances the reaction rate between $^1O_2$ and 4-CP, resulting in a much higher k value compared with the three homogeneous systems. To further elucidate the role of the catalyst's interface in the $^1O_2$ and 4-CP reaction, Co−N_2O_2/NC was added to the MB/vis-light system, and it was found that this resulted in a 5.9-fold increase in the initial degradation rate (Figure S26), consistent with our expectation. Furthermore, the differences in k values across these dye/visible-light systems indicate that certain intermolecular interactions exist between the dyes and 4-CP, which was overlooked previously.[46,47]

3.4. Enzyme-like Catalytic Mechanism. To investigate the interfacial interactions between 4-CP and the catalyst, we studied adsorption/desorption thermodynamics. Figure S27 shows that the adsorption/desorption isotherms of 4-CP on Co−N_2O_2/NC, Co−N_4/NC, Co-NPs/NC, and NC can all be well fitted to the Langmuir type-I isotherm

$$Q_e = \frac{K \times Q_m \times C_e}{1 + K \times C_e} \quad (3)$$

where Q_e is the adsorbed amount at the adsorption/desorption equilibrium. For Co−N_2O_2/NC, the Langmuir coefficient K and the capacity of adsorption Q_m are calculated to be 0.0234 and 329 ± 5 mg g^{-1}, respectively. Interestingly, the adsorption equilibrium constants and capacities of 4-CP on Co−N_4/NC, Co-NPs/NC, and NC are statistically comparable to those of Co−N_2O_2/NC. This implies that Co sites do not serve as the adsorption sites for 4-CP; otherwise, a substantial difference in 4-CP adsorption between Co−N_2O_2/NC and NC should be observed. Moreover, comparison of the ΔG, ΔH, and ΔS values for 4-CP adsorption on Co−N_2O_2/NC, Co−N_4/NC, Co-NPs/NC, and NC reveals that these values are statistically equivalent (Figure S28 and Table S5). In addition, poisoning the Co sites with KSCN resulted in no change in the equilibrium adsorption amount (Figure S29). Therefore, the NC substrate must dominate the adsorption of 4-CP. The XPS spectra in Figure S30 show that after adsorbing 4-CP, the chemical shifts of pyridine-N, pyrrole-N, and graphitic-N in Co−N_2O_2/NC undergo varying degrees of change, consistent with the above conclusion.

The nature of the interfacial interactions between 4-CP and each catalyst was studied. Figure 4a shows that the ζ-potential of each catalyst significantly decreases with increasing pH, with its isoelectric points occurring around pH = 5. This suggests that under the experimental conditions of 4-CP degradation (initial pH = 6.9, final pH = 2.8), the surfaces of these catalysts carry notable positive or negative charges. However, within the pH range of 3.0−10.9, the pH showed little effect on the equilibrium adsorption amount of 4-CP on the various catalysts (Figure 4b). This indicates that the electronic interactions between 4-CP and the NC support, rather than the Coulombic interactions, may play a significant role in the adsorption. In the in situ Fourier transform infrared (FTIR) spectrum, the peak at 1496.5 cm^{-1} is attributed to the benzene ring breathing vibration of 4-CP (Figure 4c).[41] Upon adsorption onto the catalysts' surfaces, the interfacial interaction caused a reduction in the vibrational energy of the benzene ring, leading to a red shift of this peak. The extent of the red shift follows the order Co−N_2O_2/NC > Co−N_4/NC ≈ Co-NPs/NC ≈ NC, implying that the interfacial interaction between 4-CP and Co−N_2O_2/NC is the strongest. This can be correlated with the highest k value for $^1O_2$ and the 4-CP bimolecular reaction in the Co−N_2O_2/NC system.

We further examined the relationship between the initial degradation rate R_i of 4-CP and equilibrium 4-CP concentration C_e in the Co−N_2O_2/NC/PMS system (Figure 5a). Initially, R_i increases with C_e, but at higher C_e values, it reaches a plateau. Remarkably, the correlation between R_i and C_e can be well described by the Michaelis−Menten equation (R^2 = 0.99),[48,49] as shown below

$$R_i = \frac{R_{max} \times C_e}{K_m + \times C_e} \quad (4)$$

where R_{max} represents the reaction rate when the active sites of catalyst are saturated by 4-CP, while K_m (the Michaelis constant) quantifies the affinity between the enzyme and the substrate. The K_m values for Co−N_2O_2/NC, Co−N_4/NC, and Co-NPs/NC are similar (0.98 ± 0.03 mM), indicating that their active sites are likely identical, consistent with the findings from the adsorption/desorption thermodynamics. The corresponding R_{max} values, in descending order, are 5.2 ± 0.13, 4.3

https://doi.org/10.1021/acscatal.5c01429
ACS Catal. 2025, 15, 8174−8184

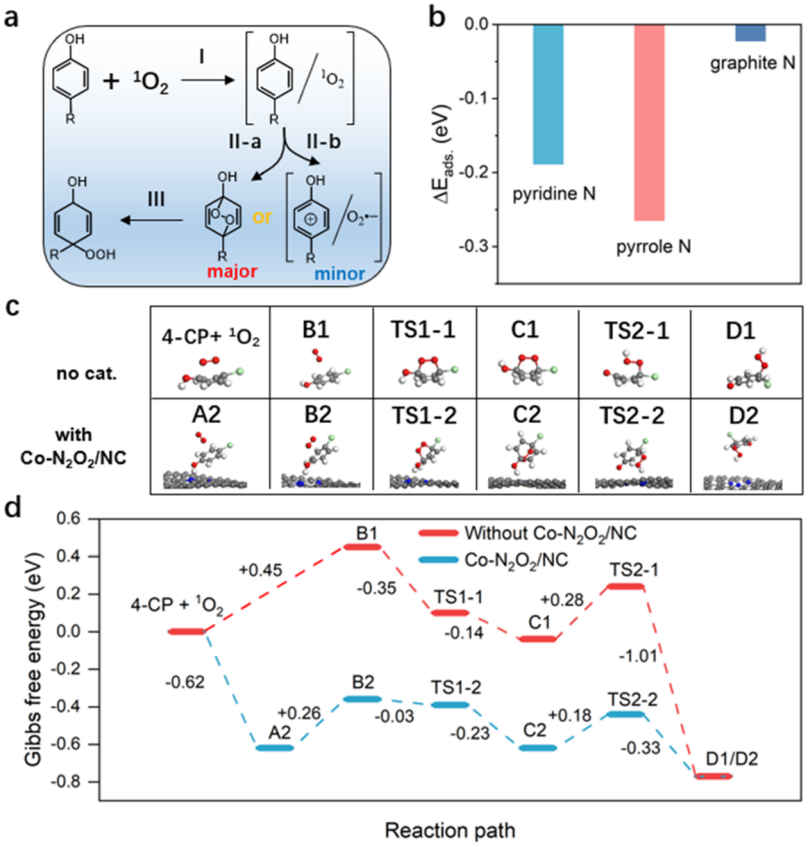

Figure 6. Theoretical calculations of the reaction mechanism. (a) The possible reaction pathways of 4-CP and $^1O_2$. (b) Adsorption energies of 4-CP on different N-sites of Co−N_2O_2/NC. (c) Structures of reaction intermediates of 4-CP and $^1O_2$. (d) The calculated energy for the reaction step and transition state based on 4-CP transformation to degradation product in a homogeneous system and at the Co−N_2O_2/NC surface.

± 0.16, and 3.9 ± 0.12 for Co−N_2O_2/NC, Co−N_4/NC, and Co-NPs/NC, respectively, which correlate with their catalytic activities.

Moreover, Figure 5b illustrates a linear correlation (R^2 = 0.96) between the R_i and Q_e of 4-CP on the various catalyst surfaces. Assuming that the apparent rate constant (k_{app}) is proportional to $R(^1O_2)$ of the catalyst, the equation can be expressed as

$$R_i = k_{app} \times Q_e \quad (5)$$

Figure 5b and eq 5 indicate that the degradation of 4-CP in the Co−N_2O_2/NC/PMS system follows a Langmuir−Hinshelwood mechanism,[50,51] where only 4-CP adsorbed onto the catalyst surface undergoes rapid degradation, indicating that the reaction is mediated at the catalyst interface. Revisiting Figure 5a, the enzyme-like relationship between R_i and 4-CP concentration suggests that 4-CP does not compete with PMS for adsorption. Otherwise, high 4-CP concentrations would inhibit PMS adsorption and activation, leading to a decrease in the R_i at elevated 4-CP concentrations.

In summary, the processes of PMS activation and 4-CP degradation can be described as follows. Initially, 4-CP in the solution bulk adsorbs onto the N-sites of Co−N_2O_2/NC and undergoes charge transfer to the NC support. Thereby, the 4-CP molecules adsorbed at the active sites of the catalyst are activated. Simultaneously, PMS is activated at the single-atom Co sites, generating $^1O_2$, for which the mechanism may be similar to the recent studies.[10,13,39] According to previous studies, the d-band center of the metal site plays a pivotal role in determining its catalytic activity toward PMS activation.[19,30] As described by the Sabatier principle, an optimal d-band center facilitates moderate PMS adsorption, thereby minimizing the energy barrier of the rate-determining step for $^1O_2$ generation.[19,32] The enhanced $^1O_2$ production observed for Co−N_2O_2/NC compared to that for Co−N_4/NC may thus be attributed to the reduced coordination symmetry and the upward shift of the d-band center toward the Fermi level, resulting from the substitution of nitrogen by oxygen atoms.[11,23] Finally, activated 4-CP rapidly reacts with $^1O_2$ at the surfaces of Co−N_2O_2/NC, resulting in oxidative degradation and mineralization.

3.5. Theoretical Calculation. Numerous studies proposed that $^1O_2$ reacts with phenols through an initial oxygenation process forming organic peroxide and subsequent degradation and mineralization.[52−54] In the initial oxygenation process, $^1O_2$ interacts with a phenol, forming a precursor complex with partial charge-transfer characteristic (Figure 6a, Step I). This is the rate-limiting step of the overall reaction. The formed charge-transfer complex may then proceed via several pathways:[42,46,52] (1) complete one-electron transfer, which yields a superoxide anion radical and a phenoxy radical (Step II-a), (2) [2 + 4] cycloaddition to form an endoperoxide (step II-b), (3) back-reaction leading only to quenching of $^1O_2$, or (4) a combination of these pathways. To understand the role of the Co−N_2O_2/NC interface in accelerating the $^1O_2$ oxidation of 4-CP, density functional theory (DFT) was used to simulate the bimolecular reaction between $^1O_2$ and 4-CP. The adsorption structure of 4-CP on the Co−N_2O_2/NC surfaces was first

https://doi.org/10.1021/acscatal.5c01429
ACS Catal. 2025, 15, 8174−8184

optimized, suggesting that the N-sites on the NC support adsorb the hydroxyl group of 4-CP (Figure S31). This is consistent with the above established conclusion that NC predominantly governs the adsorption of 4-CP. The adsorption energy of 4-CP on different N-sites of the NC support follows the order pyrrole-N > pyridine-N > graphitic-N (Figure 6b). Molecular dynamics simulations further confirmed that 4-CP remains stably adsorbed on pyrrole-N at 298 K (Figure S32). When 4-CP was adsorbed by pyrrole-N, the hydrogen atom of the hydroxyl group is in close proximity to the pyrrole-N, causing the plane of the benzene ring to slightly tilt away from parallel to the NC surface. This adsorption mode leads to a transfer of 0.04e from the NC surface to 4-CP (Figure S33), which is consistent with the in situ FTIR results (recall Figure 4c).

We subsequently simulated the reaction pathways of the oxygenation of 4-CP by $^1O_2$ both in a homogeneous system and at the NC surface (Figure 6c,d), revealing that the reaction initially forms an endoperoxide intermediate, followed by further reactions to form the peroxide. The results also indicate that regardless of the presence of an interface, the formation of a charge-transfer complex between $^1O_2$ and 4-CP is the rate-limiting step in the overall reaction. Importantly, this conclusion aligns with previous studies, which relied on the kinetic effects of substituent types,[28,42] oxidation potentials of phenolic compounds,[28] and solvent types in the homogeneous systems.[45] Therefore, the consistency validates the rationality of our DFT simulations and highlights the crucial role of charge-transfer interactions in promoting $^1O_2$ attack on the reactant. Importantly, in the homogeneous system, the activation energy of the rate-limiting step is 0.45 eV, while in the presence of the NC interface, the energy barrier decreases significantly to 0.26 eV. Surprisingly, this activation energy difference between the two systems at 298 K leads to a bimolecular reaction rate constant difference of approximately 1600 times, as estimated by $\exp(-\Delta E/RT)$, which is consistent with our experimental results. The change in the activation energy can be attributed to the electronic interactions at the NC interface (Figure S34), which not only facilitate the attack of $^1O_2$ on 4-CP but also stabilize the resulting $^1O_2$/4-CP charge-transfer complex.

3.6. Generality of the Mechanism. We also compared the degradation kinetics of various waterborne micropollutants using the Co−N_2O_2/NC/PMS system and the RB/vis-light system. The k values for the Co−N_2O_2/NC/PMS system are all significantly higher than those for the RB/visible-light systems (Figure S35). Noteworthy, although small molecules exhibit high diffusion rates, the apparent bimolecular rate constants between $^1O_2$ and contaminants in both the Co−N_2O_2/NC/PMS system and the RB/vis-light system remain below the diffusion-controlled limit ($<10^{10}$ M^{-1} s^{-1}). Therefore, interfacial catalysis remains crucial in facilitating these reactions. This indicates that the Co−N_2O_2/NC surface plays a general catalytic role in both generating $^1O_2$ and promoting the oxidation of the micropollutants by $^1O_2$ in situ.

4. CONCLUSIONS

An enzyme-like bifunctional catalyst, Co−N_2O_2/NC, is explored for the first time, effectively activating PMS to generate nearly 100% $^1O_2$ and enhancing the $^1O_2$-driven oxidative degradation of various waterborne micropollutants. The catalyst exhibits excellent recyclability and structural stability and shows great potential for scale-up applications. Notably, it demonstrates robust resistance to environmental fluctuations during the water remediation processes. The activation of 4-CP by nitrogen sites on Co−N_2O_2/NC, induced by interfacial electronic interactions, was identified as the key factor for the observed rapid interfacial kinetics. Compared to the reference catalysts, particularly the benchmark Co−N_4/NC with four coordinating N atoms, the N_2O_2 coordination of Co not only facilitated faster and more selective generation of $^1O_2$ from PMS but also enhanced the interfacial interaction with 4-CP, increasing the bimolecular reaction rate constant. The pseudo-second-order rate constant between $^1O_2$ and 4-CP in its catalyzed system is over 1400 times higher than that in uncatalyzed systems, overcoming the typically modest reactivity of $^1O_2$ and enabling its practical application for selective oxidation in real-world scenarios. Our findings may offer design principles for other transition-metal-based Fenton-like catalysts, provide new insights into micropollutant removal via $^1O_2$ in PMS-based advanced oxidation processes, and lay the groundwork for expanding the use of $^1O_2$ in a broader range of chemical transformations.

■ ASSOCIATED CONTENT

Supporting Information

The Supporting Information is available free of charge at https://pubs.acs.org/doi/10.1021/acscatal.5c01429.

Additional data on experimental section; characterizations; catalytic performance; adsorption performance; and DFT calculations (PDF)

■ AUTHOR INFORMATION

Corresponding Authors

Guanyun Zhang − *Key Lab for Colloid and Interface Science of Ministry of Education, School of Chemistry and Chemical Engineering, Shandong University, Jinan 250100, China;* orcid.org/0000-0002-6760-3354; Email: guanyzhang@sdu.edu.cn

Zhaoyong Guan − *Key Lab for Colloid and Interface Science of Ministry of Education, School of Chemistry and Chemical Engineering, Shandong University, Jinan 250100, China;* orcid.org/0000-0002-6847-5809; Email: zyguan@sdu.edu.cn

Yifeng Wang − *Key Lab for Colloid and Interface Science of Ministry of Education, School of Chemistry and Chemical Engineering, Shandong University, Jinan 250100, China;* orcid.org/0000-0002-8103-3087; Email: yifeng@sdu.edu.cn

Authors

Dezhi Kong − *Key Lab for Colloid and Interface Science of Ministry of Education, School of Chemistry and Chemical Engineering, Shandong University, Jinan 250100, China*

Yafei Fan − *Key Lab for Colloid and Interface Science of Ministry of Education, School of Chemistry and Chemical Engineering, Shandong University, Jinan 250100, China*

Feifei Wang − *Key Lab for Colloid and Interface Science of Ministry of Education, School of Chemistry and Chemical Engineering, Shandong University, Jinan 250100, China*

Fangyu Zhang − *Key Lab for Colloid and Interface Science of Ministry of Education, School of Chemistry and Chemical Engineering, Shandong University, Jinan 250100, China*

https://doi.org/10.1021/acscatal.5c01429
ACS Catal. 2025, 15, 8174−8184

Qi Zhao − *Key Laboratory of Photochemistry, Institute of Chemistry, Chinese Academy of Sciences, Beijing 100190, China*
Zhaoli Sun − *Key Lab for Colloid and Interface Science of Ministry of Education, School of Chemistry and Chemical Engineering, Shandong University, Jinan 250100, China*
Jianfei Yao − *Key Lab for Colloid and Interface Science of Ministry of Education, School of Chemistry and Chemical Engineering, Shandong University, Jinan 250100, China*
Menghui Chu − *Key Lab for Colloid and Interface Science of Ministry of Education, School of Chemistry and Chemical Engineering, Shandong University, Jinan 250100, China*
Guo Wang − *Department of Chemistry, Capital Normal University, Beijing 100048, China*
Hua Sheng − *Key Laboratory of Photochemistry, Institute of Chemistry, Chinese Academy of Sciences, Beijing 100190, China;* orcid.org/0000-0002-5605-2630

Complete contact information is available at: https://pubs.acs.org/10.1021/acscatal.5c01429

Notes

The authors declare no competing financial interest.

■ ACKNOWLEDGMENTS

The authors gratefully acknowledge the key R&D program of Shandong Province (Grant No. 2021CXGC011202), the Natural Science Foundation of Shandong Province (Grant Nos. ZR2023QB100 and ZR2024MB107), the National Natural Science Foundation of China (Grant Nos. 2276112 and 22306110), the Shandong Excellent Young Scientists Fund (Grant No. 2023HWYQ−053), the Taishan Scholars Program of Shandong Province (Grant No. tsqn20230655), and the Fundamental Research Funds of Shandong University for the financial support. The scientific calculation in this paper have been performed on the HPC Platform for Theoretical and Computational Chemistry of the School of Chemistry and Chemical Engineering of Shandong University and Hefei Advanced Computing Center.

■ REFERENCES

(1) Kachynski, A. V.; Pliss, A.; Kuzmin, A. N.; Ohulchanskyy, T. Y.; Baev, A.; Qu, J.; Prasad, P. N. Photodynamic Therapy by in Situ Nonlinear Photon Conversion. *Nat. Photonics* **2014**, *8* (6), 455−461.
(2) Idris, N. M.; Gnanasammandhan, M. K.; Zhang, J.; Ho, P. C.; Mahendran, R.; Zhang, Y. In Vivo Photodynamic Therapy using Upconversion Nanoparticles as Remote-Controlled Nanotransducers. *Nat. Med.* **2012**, *18* (10), 1580−1585.
(3) Ossola, R.; Jönsson, O. M.; Moor, K.; McNeill, K. Singlet Oxygen Quantum Yields in Environmental Waters. *Chem. Rev.* **2021**, *121* (7), 4100−4146.
(4) Gu, C.-H.; Pan, Y.; Wei, T.-T.; Zhang, A.-Y.; Si, Y.; Liu, C.; Sun, Z.-H.; Chen, J.-J.; Yu, H.-Q. Upcycling Waste Sewage Sludge into Superior Single-Atom Fenton-like Catalyst for Sustainable Water Purification. *Nat. Water* **2024**, *2* (7), 649−662.
(5) Tang, Q.; Wu, B.; Huang, X.; Ren, W.; Liu, L.; Tian, L.; Chen, Y.; Zhang, L.-S.; Sun, Q.; Kang, Z.; Ma, T.; Zou, J.-P. Electron Transfer Mediated Activation of Periodate by Contaminants to Generate $^1O_2$ by Charge-Confined Single-Atom Catalyst. *Nat. Commun.* **2024**, *15* (1), No. 9549.
(6) Mauter, M. S.; Zucker, I.; Perreault, F.; Werber, J. R.; Kim, J.-H.; Elimelech, M. The Role of Nanotechnology in Tackling Global Water Challenges. *Nat. Sustainability* **2018**, *1* (4), 166−175.
(7) Ghogare, A. A.; Greer, A. Using Singlet Oxygen to Synthesize Natural Products and Drugs. *Chem. Rev.* **2016**, *116* (17), 9994−10034.
(8) Maitra, P. K.; Bhattacharyya, S.; Hickey, N.; Mukherjee, P. S. Self-Assembly of a Water-Soluble Pd16 Square Bicupola Architecture and Its Use in Aerobic Oxidation in Aqueous Medium. *J. Am. Chem. Soc.* **2024**, *146* (22), 15301−15308.
(9) Yamaguchi, M.; Shioya, K.; Li, C.; Yonesato, K.; Murata, K.; Ishii, K.; Yamaguchi, K.; Suzuki, K. Porphyrin−Polyoxotungstate Molecular Hybrid as a Highly Efficient, Durable, Visible-Light-Responsive Photocatalyst for Aerobic Oxidation Reactions. *J. Am. Chem. Soc.* **2024**, *146* (7), 4549−4556.
(10) Zhang, L.-S.; Jiang, X.-H.; Zhong, Z.-A.; Tian, L.; Sun, Q.; Cui, Y.-T.; Lu, X.; Zou, J.-P.; Luo, S.-L. Carbon Nitride Supported High-Loading Fe Single-Atom Catalyst for Activation of Peroxymonosulfate to Generate $^1O_2$ with 100% Selectivity. *Angew. Chem., Int. Ed.* **2021**, *60* (40), 21751−21755.
(11) Wang, Z.; Almatrafi, E.; Wang, H.; Qin, H.; Wang, W.; Du, L.; Chen, S.; Zeng, G.; Xu, P. Cobalt Single Atoms Anchored on Oxygen-Doped Tubular Carbon Nitride for Efficient Peroxymonosulfate Activation: Simultaneous Coordination Structure and Morphology Modulation. *Angew. Chem., Int. Ed.* **2022**, *61* (29), No. e202202338.
(12) Li, X.; Huang, X.; Xi, S.; Miao, S.; Ding, J.; Cai, W.; Liu, S.; Yang, X.; Yang, H.; Gao, J.; Wang, J.; Huang, Y.; Zhang, T.; Liu, B. Single Cobalt Atoms Anchored on Porous N-Doped Graphene with Dual Reaction Sites for Efficient Fenton-like Catalysis. *J. Am. Chem. Soc.* **2018**, *140* (39), 12469−12475.
(13) Mi, X.; Wang, P.; Xu, S.; Su, L.; Zhong, H.; Wang, H.; Li, Y.; Zhan, S. Almost 100% Peroxymonosulfate Conversion to Singlet Oxygen on Single-Atom CoN_{2+2} Sites. *Angew. Chem., Int. Ed.* **2021**, *60* (9), 4588−4593.
(14) Gao, Y.; Wu, T.; Yang, C.; Ma, C.; Zhao, Z.; Wu, Z.; Cao, S.; Geng, W.; Wang, Y.; Yao, Y.; Zhang, Y.; Cheng, C. Activity Trends and Mechanisms in Peroxymonosulfate-Assisted Catalytic Production of Singlet Oxygen over Atomic Metal-N-C Catalysts. *Angew. Chem., Int. Ed.* **2021**, *60* (41), 22513−22521.
(15) Latch, D. E.; McNeill, K. Microheterogeneity of Singlet Oxygen Distributions in Irradiated Humic Acid Solutions. *Science* **2006**, *311* (5768), 1743−1747.
(16) Durantini, A. M.; Greene, L. E.; Lincoln, R.; Martínez, S. R.; Cosa, G. Reactive Oxygen Species Mediated Activation of a Dormant Singlet Oxygen Photosensitizer: From Autocatalytic Singlet Oxygen Amplification to Chemicontrolled Photodynamic Therapy. *J. Am. Chem. Soc.* **2016**, *138* (4), 1215−1225.
(17) Luo, Z.; Zhou, W.; Jiang, Y.; Minakata, D.; Spinney, R.; Dionysiou, D. D.; Liu, J.; Xiao, R. Bimolecular versus Trimolecular Reaction Pathways for H_2O_2 with Hypochlorous Species and Implications for Wastewater Reclamation. *Environ. Sci. Technol.* **2024**, *58* (1), 847−858.
(18) Chen, Z.; An, F.; Zhang, Y.; Liang, Z.; Liu, W.; Xing, M. Single-atom Mo−Co catalyst with Low Biotoxicity for Sustainable Degradation of High-Ionization-Potential Organic Pollutants. *Proc. Natl. Acad. Sci. U.S.A.* **2023**, *120* (29), No. e2305933120.
(19) Fan, Y.; Kong, D.; Wang, F.; Sun, Z.; Yao, J.; Chu, M.; Zhou, Y.; Tung, C.-H.; Wang, Y. Sabatier Principle-Driven Single-Atom Coordination Engineering for Enhanced Fenton-Like Catalysis. *Small* **2025**, *21*, No. 2409240.
(20) Hodges, B. C.; Cates, E. L.; Kim, J.-H. Challenges and Prospects of Advanced Oxidation Water Treatment Processes using Catalytic Nanomaterials. *Nat. Nanotechnol.* **2018**, *13* (8), 642−650.
(21) Zhen, J.; Sun, J.; Xu, X.; Wu, Z.; Song, W.; Ying, Y.; Liang, S.; Miao, L.; Cao, J.; Lv, W.; Song, C.; Yao, Y.; Xing, M. M−N_3 Configuration on Boron Nitride Boosts Singlet Oxygen Generation via Peroxymonosulfate Activation for Selective Oxidation. *Angew. Chem., Int. Ed.* **2024**, *63* (26), No. e202402669.
(22) Zhao, Y.; Yu, L.; Song, C.; Chen, Z.; Meng, F.; Song, M. Selective Degradation of Electron-Rich Organic Pollutants Induced by CuO@Biochar: The Key Role of Outer-Sphere Interaction and Singlet Oxygen. *Environ. Sci. Technol.* **2022**, *56* (15), 10710−10720.

(23) Zhao, H.-Q.; Song, J.-S.; Lu, P.; Mu, Y. Single Atom Co-Anchored Nitrogen-Doped Graphene for Peroxymonosulfate Activation with High Selectivity of Singlet Oxygen Generation. *Chem. Eng. J.* **2023**, *456*, No. 141045.
(24) Rengifo-Herrera, J. A.; Pierzchała, K.; Sienkiewicz, A.; Forró, L.; Kiwi, J.; Pulgarin, C. Abatement of Organics and *Escherichia Coli* by N, S co-doped TiO_2 under UV and Visible Light. Implications of the Formation of Singlet Oxygen ($^1O_2$) under Visible Light. *Appl. Catal., B* **2009**, *88* (3−4), 398−406.
(25) Kearns, D. R. Physical and Chemical Properties of Singlet Molecular Oxygen. *Chem. Rev.* **1971**, *71* (4), 395−427.
(26) Ogilby, P. R. Singlet Oxygen: There is Indeed Something New under the Sun. *Chem. Soc. Rev.* **2010**, *39* (8), 3181−3209.
(27) Klaper, M.; Fudickar, W.; Linker, T. Role of Distance in Singlet Oxygen Applications: A Model System. *J. Am. Chem. Soc.* **2016**, *138* (22), 7024−7029.
(28) Tratnyek, P. G.; Hoigne, J. Oxidation of Substituted Phenols in the Environment: a QSAR Analysis of Rate Constants for Reaction with Singlet Oxygen. *Environ. Sci. Technol.* **1991**, *25* (9), 1596−1604.
(29) Liu, T.; Xiao, S.; Li, N.; Chen, J.; Zhou, X.; Qian, Y.; Huang, C.-H.; Zhang, Y. Water Decontamination via Nonradical Process by Nanoconfined Fenton-Like Catalysts. *Nat. Commun.* **2023**, *14* (1), No. 2881.
(30) Fan, Y.; Chu, M.; Li, H.; Sun, Z.; Kong, D.; Yao, J.; Wang, G.; Wang, Y.; Zhu, H.-Y. Optimal Oxophilicity at the Fe-N_x Interface Enhances the Generation of Singlet Oxygen for Efficient Fenton-Like Catalysis. *Small* **2024**, *20* (43), No. 2403804.
(31) Jung, E.; Shin, H.; Lee, B.-H.; Efremov, V.; Lee, S.; Lee, H. S.; Kim, J.; Hooch Antink, W.; Park, S.; Lee, K.-S.; Cho, S.-P.; Yoo, J. S.; Sung, Y.-E.; Hyeon, T. Atomic-Level Tuning of Co−N−C Catalyst for High-Performance Electrochemical H_2O_2 Production. *Nat. Mater.* **2020**, *19* (4), 436−442.
(32) Liu, H.-Z.; Shu, X.-X.; Huang, M.; Wu, B.-B.; Chen, J.-J.; Wang, X.-S.; Li, H.-L.; Yu, H.-Q. Tailoring d-Band Center of High-Valent Metal-Oxo Species for Pollutant Removal via Complete Polymerization. *Nat. Commun.* **2024**, *15* (1), No. 2327.
(33) Lin, Y.; Wang, Y.; Weng, Z.; Zhou, Y.; Liu, S.; Ou, X.; Xu, X.; Cai, Y.; Jiang, J.; Han, B.; Yang, Z. Coordination Engineering of Heterogeneous High-Valent Fe(IV)-Oxo for Safe Removal of Pollutants via Powerful Fenton-Like Reactions. *Nat. Commun.* **2024**, *15* (1), No. 10032.
(34) Miao, J.; Song, J.; Lang, J.; Zhu, Y.; Dai, J.; Wei, Y.; Long, M.; Shao, Z.; Zhou, B.; Alvarez, P. J. J.; Zhang, L. Single-Atom MnN_5 Catalytic Sites Enable Efficient Peroxymonosulfate Activation by Forming Highly Reactive Mn(IV)−Oxo Species. *Environ. Sci. Technol.* **2023**, *57* (10), 4266−4275.
(35) Li, M.; Zhang, C.; Tang, Y.; Chen, Q.; Li, W.; Han, Z.; Chen, S.; Lv, C.; Yan, Y.; Zhang, Y.; Zheng, W.; Wang, P.; Guo, X.; Ding, W. Environment Molecules Boost the Chemoselective Hydrogenation of Nitroarenes on Cobalt Single-Atom Catalysts. *ACS Catal.* **2022**, *12* (19), 11960−11973.
(36) Wu, X.; Wang, Z.; Liu, Y.; Li, D. Polymeric Schiff Base Assisted Synthesis of Fe-N-C MFs Single-Atom Nanozymes for Discrimination and Intelligent Sensing of Tannic Acid. *Chem. Eng. J.* **2023**, *468*, No. 143638.
(37) Hu, W.; Wang, C.; Tan, H.; Duan, H.; Li, G.; Li, N.; Ji, Q.; Lu, Y.; Wang, Y.; Sun, Z.; Hu, F.; Yan, W. Embedding Atomic Cobalt into Graphene Lattices to Activate Room-Temperature Ferromagnetism. *Nat. Commun.* **2021**, *12* (1), No. 1854.
(38) Fei, H.; Dong, J.; Wan, C.; Zhao, Z.; Xu, X.; Lin, Z.; Wang, Y.; Liu, H.; Zang, K.; Luo, J.; Zhao, S.; Hu, W.; Yan, W.; Shakir, I.; Huang, Y.; Duan, X. Microwave-Assisted Rapid Synthesis of Graphene-Supported Single Atomic Metals. *Adv. Mater.* **2018**, *30* (35), No. 1802146.
(39) Weng, Z.; Lin, Y.; Guo, S.; Zhang, X.; Guo, Q.; Luo, Y.; Ou, X.; Ma, J.; Zhou, Y.; Jiang, J.; Han, B. Site Engineering of Covalent Organic Frameworks for Regulating Peroxymonosulfate Activation to Generate Singlet Oxygen with 100% Selectivity. *Angew. Chem., Int. Ed.* **2023**, *135* (43), No. e202310934.
(40) Bi, G.; Ding, R.; Song, J.; Luo, M.; Zhang, H.; Liu, M.; Huang, D.; Mu, Y. Discriminating the Active Ru Species Towards the Selective Generation of Singlet Oxygen from Peroxymonosulfate: Nanoparticles Surpass Single-Atom Catalysts. *Angew. Chem.* **2024**, *136* (17), No. e202401551.
(41) Meng, Y.; Liu, Y.-Q.; Wang, C.; Si, Y.; Wang, Y.-J.; Xia, W.-Q.; Liu, T.; Cao, X.; Guo, Z.-Y.; Chen, J.-J.; Li, W.-W. Nanoconfinement Steers Nonradical Pathway Transition in Single Atom Fenton-Like Catalysis for Improving Oxidant Utilization. *Nat. Commun.* **2024**, *15* (1), No. 5314.
(42) Thomas, M. J.; Foote, C. S. Chemistry of Singlet Oxygen—XXVI. Photooxygenation of Phenolsy. *Photochem. Photobiol.* **1978**, *27* (6), 683−693.
(43) Saito, I.; Kato, S.; Matsuura, T. Photoinduced Reactions. XL Addition of Singlet Oxygen to Monocyclic Aromatic Ring. *Tetrahedron Lett.* **1970**, *11* (3), 239−242.
(44) Matsuura, T.; Nishinaga, A.; Yoshimura, N.; Arai, T.; Omura, K.; Matsushima, H.; Kato, S.; Saito, I. Photoinduced Reactions. XXXI. Photooxidative Ring-Cleavage of Dihydric Phenols as Possible Models for Biological Oxygenation. *Tetrahedron Lett.* **1969**, *10* (21), 1673−1676.
(45) Palumbo, M. C.; Garcia, N. A. On the Mechanism of Quenching of Singlet Oxygen by Chlorinated Phenolic Pesticides. *Toxicol. Environ. Chem.* **1988**, *17* (2), 103−116.
(46) Jawad, A.; Zhan, K.; Wang, H.; Shahzad, A.; Zeng, Z.; Wang, J.; Zhou, X.; Ullah, H.; Chen, Z.; Chen, Z. Tuning of Persulfate Activation From a Free Radical to a Nonradical Pathway through the Incorporation of Non-Redox Magnesium Oxide. *Environ. Sci. Technol.* **2020**, *54* (4), 2476−2488.
(47) Choi, S. K.; Yang, H. S.; Kim, J. H.; Park, H. Organic Dye-Sensitized TiO_2 as a Versatile Photocatalyst for Solar Hydrogen and Environmental Remediation. *Appl. Catal., B* **2012**, *121*−*122*, 206−213.
(48) Lee, H. J.; Wark, A. W.; Goodrich, T. T.; Fang, S.; Corn, R. M. Surface Enzyme Kinetics for Biopolymer Microarrays: a Combination of Langmuir and Michaelis−Menten Concepts. *Langmuir* **2005**, *21* (9), 4050−4057.
(49) Kari, J.; Andersen, M.; Borch, K.; Westh, P. An Inverse Michaelis−Menten Approach for Interfacial Enzyme Kinetics. *ACS Catal.* **2017**, *7* (7), 4904−4914.
(50) Noh, J.-H.; Meijboom, R. Catalytic Evaluation of Dendrimer-Templated Pd Nanoparticles in the Reduction of 4-Nitrophenol using Langmuir−Hinshelwood Kinetics. *Appl. Surf. Sci.* **2014**, *320*, 400−413.
(51) Kiani, D.; Wachs, I. E. Practical Considerations for Understanding Surface Reaction Mechanisms Involved in Heterogeneous Catalysis. *ACS Catal.* **2024**, *14* (22), 16770−16784.
(52) Lee, J.; Von Gunten, U.; Kim, J.-H. Persulfate-Based Advanced Oxidation: Critical Assessment of Opportunities and Roadblocks. *Environ. Sci. Technol.* **2020**, *54* (6), 3064−3081.
(53) Briviba, K.; Devasagayam, T. P.; Sies, H.; Steenken, S. Selective Para-Hydroxylation of Phenol and Aniline by Singlet Molecular Oxygen. *Chem. Res. Toxicol.* **1993**, *6* (4), 548−553.
(54) Song, Q.; Niu, T.; Wang, H. Theoretical Study of the Reaction of 2, 4-Dichlorophenol with $^1O_2$. *J. Mol. Struct.:THEOCHEM* **2008**, *861* (1−3), 27−32.

https://doi.org/10.1021/acscatal.5c01429
ACS Catal. 2025, 15, 8174−8184